Observation of Ground- and Excited-State Charge Transfer at the C_{60}/Graphene Interface

Giriraj Jnawali,[†,∞] Yi Rao,[†,¥] Jonathan H. Beck,[§] Nicholas Petrone,[∥] Ioannis Kymissis,[§] James Hone,[∥] and Tony F. Heinz[*,†,§,⊥]

[†]Department of Physics, Columbia University, New York, New York 10027, United States, [§]Department of Electrical Engineering, Columbia University, New York, New York 10027, United States, and [∥]Department of Mechanical Engineering, Columbia University, New York, New York 10027, United States. [∞]Present address: Department of Physics and Astronomy, University of Pittsburgh, Pittsburgh, PA 15260, USA. [⊥]Present address: Department of Applied Physics, Stanford University, Stanford, CA 94305 and SLAC National Accelerator Laboratory, 2575 Sand Hill Road, Menlo Park, CA 94025. [¥]Present address: Department of Chemistry, Temple University, Philadelphia, PA 19122.

ABSTRACT We examine charge transfer interactions in the hybrid system of a film of C_{60} molecules deposited on single-layer graphene using Raman spectroscopy and Terahertz (THz) time-domain spectroscopy. In the absence of photoexcitation, we find that the C_{60} molecules in the deposited film act as electron acceptors for graphene, yielding increased hole doping in the graphene layer. Hole doping of the graphene film by a uniform C_{60} film at a level of $5.6 \times 10^{12}/cm^2$ or 0.04 holes per interfacial C_{60} molecule was determined by the use of both Raman and THz spectroscopy. We also investigate transient charge transfer occurring upon photoexcitation by femtosecond laser pulses with a photon energy of 3.1 eV. The C_{60}/graphene hybrid exhibits a short-lived (ps) decrease in THz conductivity, followed by a long-lived increase in conductivity. The initial negative photoconductivity transient, which decays within 2 ps, reflects the intrinsic photoresponse of graphene. The longer-lived positive conductivity transient, with a lifetime on the order of 100 ps, is attributed to photoinduced hole doping of graphene by interfacial charge transfer. We discuss possible microscopic pathways for hot carrier processes in the hybrid system.

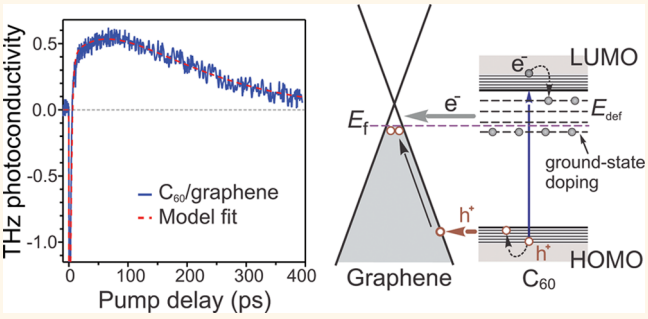

KEYWORDS: graphene · C_{60} · hybrid nanomaterials · THz time-domain spectroscopy · Raman spectroscopy · photoconductivity · interfacial charge transfer

Graphene has attracted great interest as a two-dimensional system exhibiting distinctive physical properties,[1] with many possible applications in electronic and photonic devices.[2−9] New concepts for the use of graphene in detectors and photovoltaic devices[10−12] have been explored in view of graphene's high optical transparency,[13,14] intrinsic flexibility,[15−17] and high electrical conductivity.[18−21] The combination of graphene with other nanoscale materials, such as semiconductor nanoparticles, to form novel hybrid nanostructures further expands the range of possibilities.[12,22−27]

The characteristics of such multilayer hybrid systems and the performance of devices made from them depend on interfacial electronic interactions and charge transfer. In the context of photonic applications, the response of such hybrid materials to optical excitation and the role of interfacial charge transfer are of particular importance. In this paper, we investigate a hybrid nanomaterial consisting of a solid film of C_{60} deposited on single-layer graphene. This system provides a model for charge transfer processes between graphene and a well-defined adlayer film. In addition to the attractiveness of studying an adlayer that is also comprised of sp^2-hybridized carbon, the interface is understood to be formed through relatively weak van der Waals forces and does not involve the complexity of strong chemisorption interactions.[28,29] Evidence of weak interaction was also demonstrated in the recent studies, where light hole doping was detected in graphene by adsorption of C_{60}.[30−32] Charge transfer processes involving C_{60} are of special interest because of the widespread use of C_{60}

* Address correspondence to tony.heinz@stanford.edu.

Received for review March 29, 2015 and accepted June 14, 2015.

Published online June 14, 2015
10.1021/acsnano.5b01896

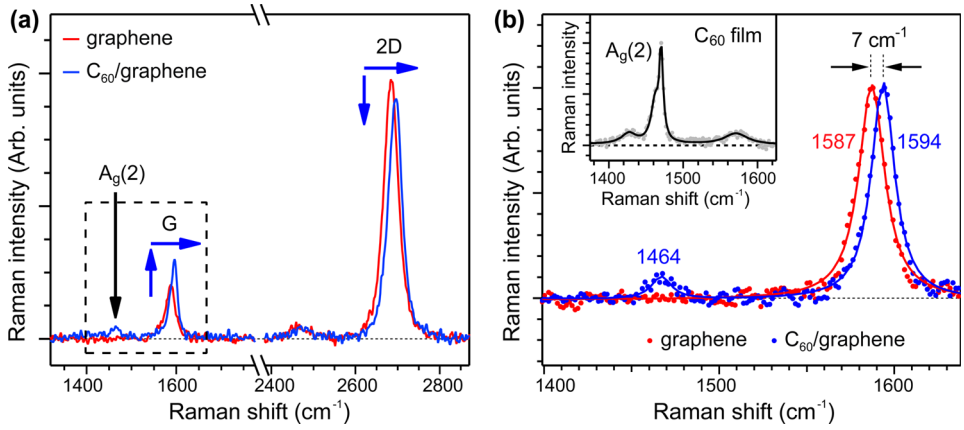

Figure 1. Charge transfer doping in pristine graphene by C_{60} deposition. (a) Raman spectra recorded for pristine graphene (red line) and after deposition of a 1 nm C_{60} film (blue line). The first-order G and second-order 2D Raman features of graphene are identified. The arrows indicate changes in the peak frequency and height upon C_{60} deposition. (b) Expanded Raman spectra from 1400−1640 cm^{-1}. The spectra are normalized by the intensity of G-mode to highlight its 7 cm^{-1} peak shift. The inset shows the Raman spectrum of a thick C_{60} film, which is dominated by the $A_g(2)$ pentagonal pinch mode around 1469 cm^{-1}. The same feature is also visible around 1464 cm^{-1} for the C_{60}/graphene sample.

derivatives as electron acceptors in organic photovoltaic devices.[33,34]

In this article, we examine both ground- and excited-state charge transfer processes at the C_{60}/graphene interface by the application of Raman spectroscopy and THz time-domain spectroscopy (THz-TDS). Unlike earlier studies, we use both of these non-contact optical probes to measure the doping parameters and study transport behavior. By probing the shift in the graphene Fermi level and change in the transport properties of graphene induced by deposition of the C_{60} film, we evaluate the amount of charge transfer doping that occurs in the hybrid system. Modest hole injection of $5.6 \times 10^{12}/cm^2$, about 0.04 charges per interfacial C_{60} molecule is identified.

For the photoexcited system, charge transfer processes and their dynamics are investigated by probing the transient conductivity of the C_{60}/graphene sample following ultrafast optical excitation with THz-TDS. The emergence of a relatively long-lived positive conductivity response, absent for photoexcitation of either of the materials separately, allows us to identify and quantify photoinduced charge transfer processes. A relatively efficient injection of photoexcited holes from the C_{60} is observed, with approximately 30% of the photoexcited holes contributing to the transient graphene conductivity. Equilibrium conditions for the system are re-established by slower electron injection into graphene, occurring on the 100 ps time scale. Combining our experimental results with knowledge of the band structure of the hybrid system, we discuss possible physical mechanisms and microscopic pathways for the different interfacial charge transfer processes.

RESULTS

Ground-State Charge Transfer. We investigated large-area single-layer graphene (SLG) samples prepared by chemical vapor deposition and transferred onto fused quartz substrates. The hybrid films were formed by thermal deposition of C_{60} films onto the surface of the SLG. (See Methods section for details of sample preparation.) Two separate experimental techniques, Raman spectroscopy and THz spectroscopy, were applied to characterize charge transfer between the C_{60} layer and the underlying graphene monolayer in the absence of photoexcitation. We first report results of the Raman study.

Figure 1 shows Raman spectra for a graphene layer in its pristine state and for the sample after deposition of a monolayer C_{60} film. The Raman spectra were recorded at five different spatial locations on the C_{60}/graphene/quartz sample and were averaged to minimize the influence of any inhomogeneity in the charge density. As expected from previous studies,[35] prominent G-mode and 2D-mode peaks of SLG appear around 1587 and 2692 cm^{-1}, respectively. The 2D peak shows a single Lorentzian profile (FWHM of 30 cm^{-1}), as expected for SLG. The D peak around 1350 cm^{-1} is barely visible. The absence of this feature, which is allowed only in the presence of localized defects, is indicative of the high quality of the graphene samples (both before and after C_{60} deposition). The Raman spectrum for SLG covered by a monolayer C_{60} film exhibits systematic differences in terms of the number, position, width, and intensity of the Raman features (Figure 1). In particular, we observe the emergence of a Raman mode at 1464 cm^{-1} for the C_{60}-covered graphene sample. This feature arises from the C_{60} molecules, as can be seen by a comparison with a bulk (100 nm) C_{60} film [inset of Figure 1b], and is attributed to the C_{60} A_g (2) pentagonal pinch mode.[36]

Inspection of the Raman spectra of the graphene G and 2D features in Figure 1 reveals that both modes are slightly blue-shifted and also exhibit changes in

TABLE 1. Transport Parameters[a]

Quantity / Method	N_{gr} ($\times 10^{12}$ cm^{-2})	E_f (gr) (meV)	Γ_{gr} (cm^{-1})	$N_{C_{60}/gr}$ ($\times 10^{12}$ cm^{-2})	$E_f(C_{60}/gr)$ (meV)	$\Gamma_{C_{60}/gr}$ (cm^{-1})	$\lvert N_{C_{60}/gr} - N_{gr}\rvert$ ($\times 10^{12}$ cm^{-2})
Raman	2.2 ± 0.5	-190 ± 20	-	7.8 ± 1	-360 ± 20	-	5.7 ± 0.5
THz-TDS	3.2 ± 1	-230 ± 40	133	8.7 ± 2	-380 ± 40	70.7	5.5 ± 1

[a] Inferred hole density N, Fermi energy E_f, and scattering rate Γ for pristine graphene samples and C_{60}/graphene hybrid layers as obtained by Raman spectroscopy and THz-TDS measurements.

the intensity and width upon C_{60} deposition. Analysis of the position of these two features allows us to estimate the carrier density in the samples.[37−40] The blue-shifted position of the 2D peak relative to that for undoped graphene is indicative of additional hole doping.[39,40] For a more quantitative analysis of the level of hole doping, we make use of the shift of the G-mode frequency ω_G with the Fermi energy E_F, as summarized by the relation[37,39,41] $\omega_G - 1580$ cm^{-1} = (42 cm^{-1}/eV) $|E_F|$. From this expression, we estimate the Fermi energies for the pristine and C_{60}-covered graphene as $E_F^{gr} = -190 \pm 20$ meV and $E_F^{C_{60}/gr} = -360 \pm 20$ meV, respectively. In terms of the observed shift in the G-mode frequency upon C_{60} deposition, the value of 7 ± 1 cm^{-1} implies a change in the graphene Fermi energy of 170 meV. The quoted values correspond to spatial averages over the sample, with error bars based on the observed fluctuation and uncertainty in determination of the position of the Raman peaks of ± 1 cm^{-1}.

From the corresponding Fermi energies, we can also estimate the density of holes in the pristine SLG and the C_{60}-covered SLG regions. We use the relation between the doping density N and the Fermi level E_F for graphene of $|E_F| = \hbar v_F (\pi |N|)^{1/2}$, where v_F is the Fermi velocity of the linear bands; we neglect the (slight) influence of finite temperature for these doping levels. The corresponding charge densities for the pristine and C_{60}-covered graphene are shown in Table 1 using a Fermi velocity of $v_F = 1.1 \times 10^6$ m/s (ref 42). The hole doping of graphene from the C_{60}-layer is found to be 5.7×10^{12} cm^{-2}. We note that the graphene charge density inferred from the Raman G-mode frequency may be altered by the effects of strain.[43] The possible influence of strain should not, however, influence our determination of charge transfer from the C_{60} layer, since the level of strain in the graphene films is not expected to change upon C_{60} deposition. Below we also confirm the level of hole doping of graphene by C_{60} using the independent technique of THz spectroscopy, which is insensitive to strain.

As a second experimental technique to probe the charge transfer process upon C_{60} deposition, we have applied THz time-domain spectroscopy (see Methods) to determine the hole density of the samples. Figure 2a displays waveforms of the measured THz electric field under three different experimental conditions, probing a pristine SLG film on the quartz substrate, a C_{60} film on the substrate without a graphene layer, and the hybrid SLG film covered by a C_{60} film. We see that there is no significant THz conductivity of the C_{60} film alone. The reduction in the THz field for pristine SLG and the SLG covered by C_{60}, however, indicates the presence of a measurable conductivity. The conductivity of the graphene sample increases upon deposition of the C_{60} film, corresponding to the observed reduction in the transmitted THz electric field.

We have analyzed these results to extract the frequency-dependent complex sheet conductivity $\sigma(\omega)$ of the samples using the approach described in the Methods section. Figure 2b,c shows the inferred conductivity spectra for the graphene and C_{60}/graphene samples. The sheet conductivity of the pristine SLG sample at low frequencies is nearly 20 G_0, where $G_0 = 2e^2/h = 77.5$ μS denotes the quantum of conductance. The conductivity spectrum of the pristine graphene sample shows a rather flat response with frequency, indicating a high scattering rate in our graphene samples compared to the probed THz spectral range, as is typical for similar CVD-grown graphene.[44−47] In contrast to the pristine graphene, the C_{60}-covered graphene exhibits a higher conductivity of 43 G_0 at low frequencies and a stronger frequency dependence of the response. The THz conductivity does not change meaningfully as the C_{60} coverage is increased above a monolayer, as we have checked for films up to 50 nm in thickness (not shown). This indicates that intrinsic conductivity within the C_{60} film can be neglected and also that the charge transfer process is defined by the first monolayer of deposited C_{60}.

To analyze the transport behavior in greater detail, we compare the experimental complex conductivity spectra with predictions from a simple Drude form:[48−52]

$$\sigma(\omega) = \frac{D}{\pi} \frac{1}{(\Gamma - i\omega)} \quad (1)$$

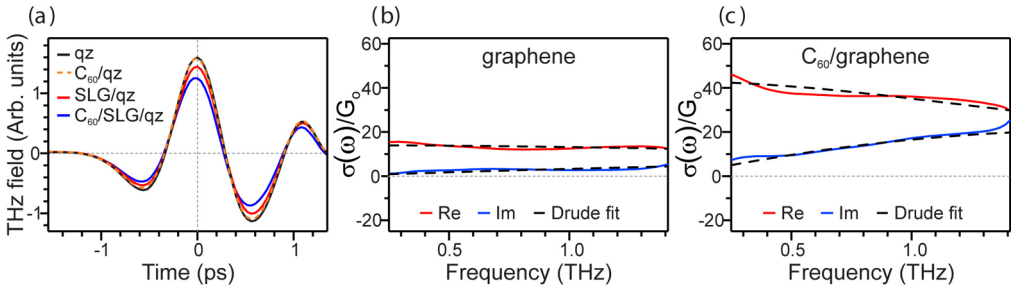

Figure 2. THz response of pristine and C_{60} deposited graphene. (a) Time-domain waveforms of the transmitted THz pulse for a pristine graphene layer (SLG/qz) and 1 nm C_{60} film on graphene (C_{60}/SLG/qz), as well as a reference signal for a blank fused quartz substrate (qz). (b and c) The corresponding complex sheet conductivities $\sigma(\omega)$ for the pristine graphene layer and the C_{60}-covered graphene layer, given in units of the quantum of conductance $G_0 = 2e^2/h$. Fits to the Drude model (discussed in the text) for both the real and imaginary parts of the conductivity are shown by dashed lines.

Here Γ is the carrier scattering rate (also quoted in units of cm^{-1} for $\Gamma/2\pi c$, where c is the speed of light in vacuum), and the parameter D is the Drude weight. For both the pristine graphene samples and the C_{60}-covered graphene [Figure 2b,c], the Drude model fits the measured values of the complex conductivity adequately within the spectral range of 0.25−1.45 THz where we have sufficient power for reliable measurements. From the fits to the Drude model, we obtain the values for the Drude weight D and the scattering rate Γ for each sample.

For the case of the pristine graphene samples on insulating substrates, the THz response clearly originates from that material. For the C_{60}/SLG sample, the Raman measurements described above have revealed increased doping in the graphene layer, and we attribute the increase in the observed conductivity to the greater doping of the graphene layer. For conductivity arising from transport in graphene with carrier density N, the Drude weight is given by $D = (v_F\ e^2/\hbar)(\pi N)^{1/2}$.[53−55] Here e denotes the electronic charge, and we have neglected the effect of finite temperature, since the relevant Fermi energies are all large compared to the thermal energy at room temperature. This expression allows us to convert the measured Drude weight D into the graphene carrier density N.

In Table 1, we present the inferred parameters for the doping level (in terms of the carrier density and Fermi energy) and the scattering rate, both for the case of pristine graphene and for C_{60}/graphene, as determined by THz measurements. The uncertainty was defined by the variation in the Drude model fits for data recorded at several different positions on the sample. On the basis of this analysis, we find that deposition of C_{60} on graphene leads to a downshift of the Fermi energy of the hole-doped graphene by 160 meV, with an increase in the hole density of 5.5×10^{12} cm^{-2}. We also note that the increased doping from C_{60} deposition is accompanied by an appreciable decrease in scattering rate of the carriers, dropping from 133 to 70.7 cm^{-1}.

Excited-State Charge Transfer. We now investigate the change in conductivity induced in the C_{60}/graphene sample by excitation with ultrashort 400 nm (3.1 eV) laser pulses. We examine both the dynamics directly in the time domain and the evolution of the THz spectral response at different time delays. To interpret the results, we provide a comparison with the response observed both for the pristine graphene and for a film of C_{60} deposited on the fused quartz substrate without graphene, *i.e.*, for the two separated components of the hybrid film.

Figure 3a shows the time traces of the photo-induced change in THz conductivity $\Delta\sigma_\tau$ as a function of delay time τ of the probe with respect to the laser excitation pulse for the C_{60}/graphene sample. Also presented are reference signals for a pristine graphene layer and for a layer of C_{60} deposited on the fused quartz substrate without graphene. These measurements were performed directly in the time domain by monitoring the change in the THz probe field at the peak of the THz waveform. A more detailed spectral analysis of the transient THz response is presented below, but this simple measurement is meaningful in view of the relatively weak spectral variation of the THz response.

Let us first consider the response of the reference samples. For the pristine graphene layer, the THz conductivity decreases on a time scale of 1 ps and recovers back to the unexcited level within a few ps ($\tau_1 \sim 2.5$ ps). For C_{60} layers without graphene, we observe a short-lived positive photoconductivity transient: the conductivity increases immediately after photoexcitation and then relaxes within a few ps, showing a typical biexponential decay, as reported in previous studies.[56]

For the case of C_{60}/graphene sample, we see the emergence of completely different dynamic behavior. In addition to the short-lived early time transient present in both the pristine graphene and C_{60} layers, we observe a transient conductivity response that lasts for hundreds of picoseconds [Figure 3b]. The initial transient corresponds to a decrease in conductivity as found for pristine graphene.[57] This indicates that dominant initial response arises from that of the

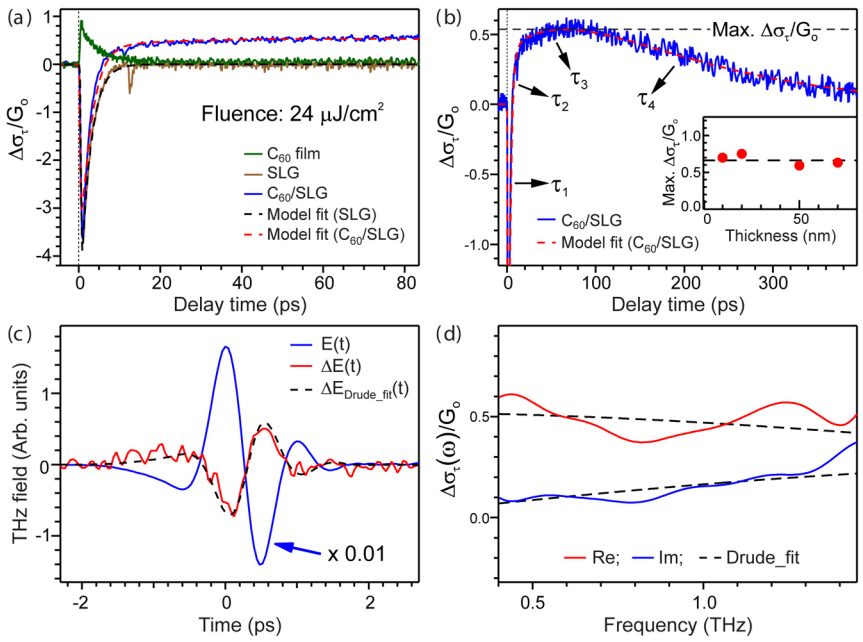

Figure 3. Dynamics of photoinduced THz conductivity and spectral response. (a) The temporal evolution of photoinduced change in conductivity $\Delta\sigma_\tau$ for pristine graphene (brown line), graphene with a 50 nm C_{60} film (blue line), and graphene with 100 nm C_{60} film (green line) after excitation with 400 nm laser pulses as measured at the peak of the THz waveform. The peaks at 15 ps arise from a reflected beam from the back of the substrate and have no physical significance. The black and red dashed lines are the fits based on the convolution of the instrumental response function with a multiexponential decay, as described in the text. Here and below, $\Delta\sigma_\tau$ is given in units of the quantum of conductance $G_0 = 2e^2/h$. (b) Time evolution of $\Delta\sigma_\tau$ for graphene with a 50 nm C_{60} film, measured up to a delay of 400 ps, together with the fit described in the text. The inset shows the maximum increase of $\Delta\sigma_\tau$, recorded at a delay of 85 ps as a function of the thickness of the C_{60} film. (c) The THz electric field $E_0(t)$ transmitted through the C_{60}/SLG sample (blue line) together with the pump-induced THz waveform, $\Delta E_0(t)$ (red line) at a fixed pump−probe delay of $\tau = 85$ ps. (d) The photoinduced change in the complex THz conductivity $\Delta\sigma_\tau(\omega)$ of the C_{60}/SLG layer extracted from the pump-induced THz response in (c). The black dashed lines are fits based on a Drude response of C_{60}/graphene both before and after photoexcitation. The Drude fit is converted into a predicted time-domain waveform $\Delta E_{\text{Drude\_fit}}(t)$, which, as shown in (c) with dashed line, agrees well with the experimental data for the pump-induced THz response.

graphene response, rather than from the C_{60} layer alone, as expected from the strength of the individual responses. The new positive conductivity response of the C_{60}/graphene system shows a rapid initial rise, followed by a slower increase to peak conductivity at around 90 ps and a slow recovery back to the unperturbed conductivity. We fit the transient conductivity with a multiexponential function convolved with the negative conductivity response of isolated graphene. We extract the time constants for the rapid initial rise ($\tau_2 \sim 0.8$ ps), the subsequent slower increase ($\tau_3 \sim 40$ ps), and final relaxation of the photoconductive response ($\tau_4 \sim 120$ ps).

To understand the origin of the signal, we carried out measurements with C_{60} films of varying thicknesses (10, 20, 50, and 70 nm) deposited on graphene/quartz substrates. All samples showed similar dynamics and a nearly constant positive photoconductivity maximum [see inset of Figure 3b]. This result shows that the conductivity transient is determined by the interfacial region, with the first few layers of C_{60} defining the photoinduced response. For comparison, we examined the effect of exciting the sample with laser pulses at 800 nm (photon energy of $h\nu = 1.5$ eV). In this case, the photoinduced response was essentially that of the pristine graphene sample and did not display a photoinduced increase in conductivity. (Please see Supporting Information.)

To obtain more quantitative information about the photoinduced response of the C_{60}/graphene system, we also determined the photoinduced change in the THz conductivity spectrum. Figure 3c shows results for the differential change in the transmitted THz waveform $\Delta E_\tau(t)$ at a time delay of $\tau = 85$ ps where the photoinduced conductivity is at its maximum. From these results we deduce the photoinduced change in the frequency-dependent THz conductivity $\Delta\sigma_\tau(\omega)$ as shown in Figure 3d.

As a simple phenomenological model of the transient response, we assume that both the initial (unpumped) response of the C_{60}/graphene layer $\sigma(\omega)$ and its response after photoexcitation $\sigma_\tau(\omega)$ can be described by a Drude form. Writing each of these Drude response terms with its own weight and scattering rate, we then have a differential change in the conductivity of

$$\Delta\sigma_\tau(\omega) = \sigma_\tau(\omega) - \sigma(\omega) = \frac{D_\tau}{\pi}\frac{1}{(\Gamma_\tau - i\omega)} - \frac{D}{\pi}\frac{1}{(\Gamma - i\omega)} \quad (2)$$

where D denotes the initial C_{60}/graphene Drude weight, D_τ denotes the Drude weight at a time delay τ after

photoexcitation, with analogous designations for scattering rates Γ and Γ_τ. We can then fit the experimentally measured differential change in the THz conductivity $\Delta\sigma_\tau(\omega)$. We take values for D and Γ directly from the THz measurements on the unexcited C_{60}/graphene sample and treat D_τ and Γ_τ as adjustable parameters. The dashed line in Figure 3d shows the best-fit result in the frequency domain, with the corresponding quantities in the time domain presented in Figure 3c. The fit shows good overall agreement, given the simplicity of the model.

The inferred parameters for the photoexcited system are then given by $D_\tau = (9655 \pm 20)\ G_0\ \mathrm{cm}^{-1}$ and $\Gamma_\tau = 70.9 \pm 0.2\ \mathrm{cm}^{-1}$. These values correspond to increases of the Drude weight of $\Delta D \cong 120\ G_0\ \mathrm{cm}^{-1}$ and of the scattering rate of $\Delta\Gamma \cong 0.2\ \mathrm{cm}^{-1}$. While the photoinduced changes in both of these parameters are small, the fractional increase in the Drude weight is several times that of the scattering rate. Interpreting the induced change in the Drude weight as arising from the graphene layer alone, we infer an increase in the carrier density of $\Delta N_\tau = N_\tau - N = 2 \times 10^{11}\ \mathrm{cm}^{-2}$. As we discuss below, we ascribe this increase in charge density to hole injection from the C_{60} layer into graphene. On the basis of the 1.4% absorption of a 1 nm thick C_{60} layer at the 400 nm pump wavelength (see Supporting Information), we estimate that 30% of the holes produced in the C_{60} layer are transferred to the graphene layer.

DISCUSSION

In our study, we applied two very different experimental techniques, namely Raman spectroscopy and THz-TDS, to examine charge transfer processes occurring upon deposition of C_{60} films on single-layer graphene. As shown in Table 1, within the experimental uncertainties, the two methods give consistent values for the charge density for the pristine and C_{60}-covered graphene films. For our CVD-grown graphene samples with initial (unintentional) hole doping, we observe a significant increase in hole density upon C_{60} deposition, corresponding to charge transfer of $5.6 \times 10^{12}\ \mathrm{cm}^{-2}$. This level of charge transfer corresponds to approximately 0.04 electrons for every C_{60} molecule in the first monolayer (*i.e.*, a monolayer of a closely packed hexagonal lattice[28,58,59]).

The agreement between the two measurements eliminates some questions associated with the application of either of them separately. In particular, the Raman data could be influenced by extrinsic factors such as strain, while the THz measurements do not specifically determine that the conductivity is associated with the graphene response, as opposed to the response of the C_{60} film. Also, the THz measurements do not directly determine the sign of the charge doping. Taken together, however, the pair of techniques provides a reliable determination of the hole doping induced in graphene after deposition of the C_{60} film. We should also point out that background effects made it difficult to apply the Raman technique for thicker C_{60} films. The THz measurement, on the other hand, showed that change transfer was largely uninfluenced by C_{60} layers beyond the first monolayer deposited.

A further noteworthy observation about the nature of the charge transfer process comes from the THz data. The THz spectra yield both the Drude weight (hence, the carrier density) and the scattering rate. From these factors, we determine the carrier mobility as $\mu = \sigma(0)/Ne$. We find $\mu_{gr} \simeq 2200\ \mathrm{cm}^2/(\mathrm{V\ s})$ prior to C_{60} deposition increases to $\mu_{gr} \simeq 3700\ \mathrm{cm}^2/(\mathrm{V\ s})$ after C_{60} deposition. Since the DC conductivity of graphene $\sigma(0)$ scales with density as $\sqrt{N}$, we expect that the mobility of the carriers in graphene will decrease with increasing N for a constant scattering rate. In this case, however, there is a sufficiently large decrease in the scattering rate Γ upon C_{60} deposition that the mobility increases, despite the increased doping density. The decrease in scattering rate with C_{60} deposition presumably reflects the improved screening of charged impurity scattering.[60] The significant increase in graphene hole concentration combined with the improved carrier mobility indicates that C_{60} can act as an effective contact dopant for graphene.

We now briefly examine the microscopic mechanism underlying the interfacial charge transfer process that leads to C_{60} hole doping, considering the interfacial energy level alignment between graphene and the C_{60} states. On the basis of photoemission data,[32] the HOMO level in the C_{60} lies more than 2 eV below the Dirac point in graphene and thus cannot donate charges to the graphene layer. For the unoccupied levels of the C_{60} film, the LUMO lies significantly above the Dirac point,[32,34] precluding charge capture from graphene. Charge transfer between the graphene and C_{60} film is therefore attributed to the role of defect states in the C_{60} films lying between the HOMO and LUMO levels. Generally speaking, charge transfer could arise either from the occupied C_{60} states lying above the graphene Fermi energy or empty C_{60} states lying below it. Since we observe hole doping of the graphene, the relevant process must be the capture of graphene electrons by unoccupied trap states in C_{60} located below the Fermi energy in graphene. We associate these levels in the C_{60} film with the influence of oxygen exposure, which is known to lead to trap states.[61,62] The relatively modest charge transfer associated with the C_{60} films (0.04 electron for each C_{60} molecule in the first layer) is compatible with the role of defect states. The observed hole doping in this system is, for example, considerably smaller than that for the case of C_{60} deposited on metallic films such as Al(111),[63] Ag(111),[64] and Au(111),[65] which involve 0.2−0.8 electrons per C_{60} molecule.

A striking feature of photoexcitation of the C_{60}/graphene system is the induction of a long-lived positive photoconductivity response. We consider its physical origin and differentiate it from signals from the individual materials shown in Figure 3a. The initial negative photoconductivity transient of the C_{60}/graphene system is attributed primarily to the graphene photoresponse. The transient decrease in graphene conductivity from photoexcitation has been investigated previously[57,66,67] and identified as arising from a rapid heating effect in which there is an elevated carrier scattering rate prior to cooling of the initial nonequilibrium distribution of carriers and optical phonons. A weak positive photoconductive response from the C_{60} film may also contribute to the C_{60}/graphene signal during the first few picoseconds, but this term is dominated by the graphene response. Carriers generated in the C_{60} layer relax within a few picoseconds due to geminate pair recombination,[56] with only a minor fraction of the carriers escaping the geminate process and contributing to the conductivity transient up to tens of picoseconds. On the basis of measurements of the signal for the isolated C_{60} layer, this contribution to the conductivity is negligible.

We must therefore attribute the long-lived positive photoconductive response to the mutual interaction of the C_{60} and graphene layers. What is not clear *a priori* is whether the increased conductivity arises from a change in the response of graphene induced by charge transfer from the photoexcited C_{60} layer or, conversely, a change in the response of the C_{60} layer induced by charge transfer from the photoexcited graphene. Here we argue that the former is dominant. The carrier mobility in graphene far exceeds that of the C_{60} film,[68,69] so we anticipate a greater response from injection of a carrier into graphene than into the C_{60} film. In addition, the photoinduced conductivity spectrum in Figure 3d shows a Drude-like behavior similar to that of the unexcited C_{60}/graphene sample, with little change in the carrier scattering rate. This would not be expected if there were a significant contribution to the THz conductivity from the C_{60} layer, which would exhibit transport through a disordered network.

Further evidence supporting the picture of charge injection from C_{60} into graphene is provided by a comparison of the response for photoexcitation of the C_{60}/graphene system by laser excitation with 800 nm pulses. (See Supporting Information.) For this case, with 1.5 eV photons, carriers are generated only in graphene. In this case, the long-lived photoconductive response disappears.

There are, generally speaking, two possible scenarios for charge injection from the photoexcited C_{60} layer into graphene, either hot electron or hot hole injection. In either case, we would expect very rapid relaxation

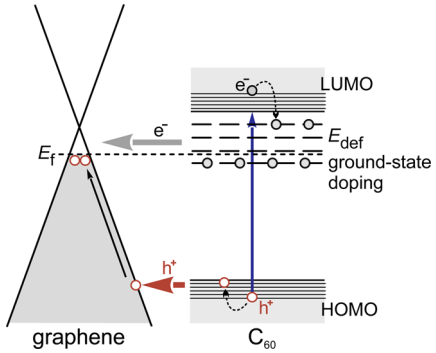

Figure 4. Electronic states in C_{60}/graphene and photoexcited charge transfer processes. Electron and hole transfer mechanism across the C_{60}/graphene interface based on the level alignment for C_{60}/graphene found in refs 32 and 34. The blue arrow indicates the initial photoexcitation of the C_{60} electronic bands by a 3 eV photon pulse. For clarity, the direct excitation of carriers and their rapid subsequent relaxation in graphene are not shown. In the C_{60} film, photoexcited electrons are rapidly trapped at defects (dotted arrows). Photoexcited holes can, however, be injected into the graphene (thick dark red arrow), where they quickly relax to the Fermi level (black arrow in the graphene bands). On a slower time scale, electron transfer from the C_{60} layer into graphene (gray arrow) neutralizes the injected holes, and the conductivity returns to its initial value as equilibrium is re-established.

of the extra charge carrier to the Fermi energy of graphene, in view of the absence of a band-gap in graphene. On the basis of the fact that the graphene is initially hole doped and that the conductivity *increases* upon photoexcitation, we conclude that the dominant initial charge transfer into graphene is hole injection. The origin of the rise in conductivity with faster ($\tau_2 \sim 0.8$ ps) and slower ($\tau_3 \sim 40$ ps) contributions is unknown, but may reflect the relaxation dynamics of hot holes in the C_{60} film.

The experimental finding of increased hole concentration in graphene following photoexcitation of the C_{60} poses the question of why electron injection from the photoexcited C_{60} is less efficient. This difference may reflect the role of midgap defect states, such as oxygen vacancies,[62,69] in the C_{60} that trap the photoexcited electrons and render them less available for transfer into the graphene. We note, however, that after a time $\tau_4 \sim 120$ ps, the additional holes injected into graphene are eliminated by electron injection from the C_{60} film (or, equivalently, by hole recapture by the C_{60}). We also should comment on the possible role of energy transfer, as opposed to charge transfer processes, from the C_{60} layer to graphene. Through a Förster mechanism, an electron–hole pair in the C_{60} layer could be annihilated, while simultaneously producing an electron–hole pair in graphene. Evidence for such processes has been obtained for quantum dots on graphene.[70] We do not believe that such processes play a significant role in the present experiment. The expected net effect of such an energy transfer processes on the graphene conductivity

would be slight because of the rapid relaxation of the carriers in graphene, as well as of the opposite sign compared to the observed long-lived increase in the graphene conductivity by the photoexcited C_{60}.

Our understanding of experimental evidence of charge injection processes is also supported by recently measured interfacial band alignment between the graphene and solid C_{60} film.[32] On the basis of this picture, we draw a simplified diagram of basic charge transfer processes in Figure 4. According to this diagram, prior to photoexcitation, we would expect neither electron nor hole transfer between the C_{60} layer and graphene from the HOMO and LUMO states. As discussed above, defect states could facilitate the observed equilibrium hole doping of graphene by C_{60}. The diagram also shows the possibility of hot hole injection from the C_{60} HOMO band, as well as hot electron injection from the C_{60} LUMO band. On the basis of this band alignment, with the Dirac point of graphene closer to the LUMO band than to the HOMO band, the higher density of states for hole injection into graphene compared to that for electron injection may also be a factor favoring the former.

CONCLUSION

We have investigated interfacial charge transfer in C_{60}/graphene hybrid structures. Both Raman spectroscopy and THz time-domain spectroscopy measurements show that in equilibrium the C_{60} layer acts as an electron acceptor, leading to hole doping of the graphene with the injection of approximately 0.04 holes for each C_{60} molecule at the surface and a downshift of graphene Fermi level by 160 meV. This doping is accompanied by an increase in the graphene carrier mobility. After photoexcitation, the transient THz response revealed a rapid (~1 ps) increase in the graphene conductivity arising from further (hot) hole injection from the C_{60} film. The C_{60}/graphene system relaxes to equilibrium with back charge transfer on the time scale of 100 ps. The charge transfer process occurs only from C_{60} molecules near the interface and exhibits an injection efficiency of ~0.3. This experiment demonstrates the importance of charge transfer processes at graphene interfaces, both in equilibrium and under photoexcitation, as well as the utility of THz spectroscopy in following these processes in real time.

METHODS

Sample Preparation and Characterization. The large-area, single-layer graphene (SLG) samples examined in this study were synthesized by chemical vapor deposition (CVD) on Cu foil following standard processing conditions.[71] Graphene films of approximately 15 mm × 20 mm size were transferred onto quartz substrates using a dry-transfer procedure[72] in which the Cu foil was removed by etching in a ferric chloride ($FeCl_3$) solution. Prior to the graphene transfer process, the quartz substrates were cleaned in an oxygen plasma.

Before deposition of C_{60}, regions of the SLG films were masked in order to maintain areas of graphene free of C_{60} to allow optical characterization of both pristine graphene and graphene covered with C_{60} on the same sample. The C_{60} films were deposited onto the graphene layers by thermal evaporation (Ångstrom Engineering Åmod physical vapor deposition system with stage rotation enabled). The deposition rate was 0.05 nm/s and the vacuum was held to $\sim 10^{-7}$ Torr. The deposition rate and layer thickness of C_{60} were monitored *in situ* by a calibrated quartz crystal microbalance. The C_{60} material, rated at >99.5% purity, was purchased from Lumtec (LT-S903, Luminescence Technology Corp., Taiwan) and was used as received.

The morphology of C_{60} films both on pristine and graphene-covered quartz substrates was characterized by atomic force microscopy (AFM). Measurements were conducted in air on a Veeco Enviroscope AFM using Si cantilevers operating in tapping mode. The root-mean-square (RMS) surface roughness was determined from AFM height images obtained over an area of 1 μm^2 (see Supporting Information). Typical RMS roughness of thicker films (thickness >10 nm) on both regions is in the order of 2 nm for the (1 × 1) μm^2 scan size. Interestingly, a single layer (~1 nm) C_{60} film is found to exhibit a much smoother profile on the graphene region than on the bare quartz region. (See Supporting Information.) This behavior might be related to the increased diffusivity of C_{60} molecules on the graphene surface.[73,74] We examined C_{60} films ranging in thickness from 1 to 100 nm for the THz measurements. Single-layer C_{60} films (~1 nm thickness) were prepared for the Raman measurements to avoid strong signals from the bulk C_{60} response. The interfacial characteristics seen in the measurements were similar in all cases. This suggests that the monolayer-thick film was relatively homogeneous and that no strong clustering effects of the C_{60} molecules were present in our samples.

Raman spectroscopy was applied to characterize film quality and also to evaluate the charge density in graphene. The measurements were performed using a commercial Raman microscope (Renishaw InVia) with 532 nm laser excitation. The spectral resolution of the instrument was approximately 1 cm^{-1}. To avoid sample degradation from heating effects, the laser power was maintained well below 1 mW during the measurements. These and all other measurements were performed at room temperature.

Photoexcitation and THz Time-Domain Spectroscopy. Our measurements made use of optical excitation of the sample by a femtosecond laser pulse and probing of the THz response using a time-domain spectroscopy approach. The laser excitation for both the optical pumping and THz time-domain spectrometer was provided by a regeneratively amplified, modelocked Ti:sapphire laser, which produced 2-mJ, 120 fs pulses at a repetition rate of 1 kHz and a center wavelength of 800 nm. Most of the measurements were performed using photoexcitation at 400 nm (3.1 eV) by frequency doubling the laser excitation in a β-barium borate (BBO) crystal.

The generation and detection of THz pulses and the synchronization with optical pulses in an optical pump-THz probe setup has been described elsewhere in detail.[57,75] Here we summarize key aspects of the current experiment. The THz pulses were generated from the 800 nm femtosecond laser pulses by means of optical rectification in a 1 mm thick ZnTe(110) crystal.[76] The emitted THz pulses were collimated and focused by a pair of off-axis parabolic mirrors onto the sample. The size of the THz beam on the graphene sample was about 2 mm. After passing through the sample, the diverging THz radiation was collimated and focused by another pair of off-axis parabolic mirrors onto another 1 mm thick ZnTe(110) crystal, which permitted detection of the THz field by means of free-space electro-optic sampling (EOS).[76−78] The THz electric

field was detected with an optical sampling beam at a variable delay time. The measurements were performed using a lock-in amplifier synchronized with an optical chopper that modulated either the THz beam or the pump beam at a frequency of 500 Hz. In the former configuration, we measured the transmitted THz waveform; in the latter, we obtained the differential change of the THz waveform induced by optical excitation of the sample. We note that the THz absorption by the quartz substrate over the relevant spectral range was negligible, permitting transmission measurements to be performed. For studies of the photo-induced response of the C_{60}/graphene, the 400 nm pump pulses irradiated the sample at an angle of 5° from surface normal. To ensure the probing of a homogeneously photoexcited region, a pump beam diameter of 5 mm was used, significantly larger than the 2 mm spot size of the THz beam. The temporal evolution of the photoinduced response could be traced by varying the arrival time of the pump pulse and the THz probe pulse with an optical delay line. The THz beam path was enclosed and purged with dry nitrogen to avoid absorption by water vapor.

Extraction of THz Conductivity and THz Photoconductivity. The conductivity of the samples was determined using THz-TDS.[75] To extract the conductivity of the unexcited sample (for both graphene and C_{60}/graphene), we recorded the time-dependent electric fields of the THz wave transmitted through both samples. We converted these waveforms into the corresponding (complex) frequency-domain fields, *i.e.*, $E_{gr}(\omega)$ and $E_{C_{60}/gr}(\omega)$, for graphene and C_{60}/graphene, respectively, where ω denotes the angular frequency of the THz radiation. Applying the standard thin-film approximation,[79,80] we determined the frequency-dependent complex sheet conductivity for graphene $\sigma_{gr}(\omega)$ from the measured transmission spectra using

$$\frac{E_{gr}(\omega)}{E_0(\omega)} = \frac{n+1}{n+1+Z_0\sigma_{gr}(\omega)} \quad (3)$$

and similarly for the C_{60}/graphene sample. Here $E_0(\omega)$ corresponds to the electric field measured passing through the substrate in a region without graphene, $Z_0 \approx 377\ \Omega$ is the impedance of free space, and n is the refractive index of the fused quartz substrate. We treat the THz refractive index of the substrate as dispersion free with $n = 1.9$[81,82] and have not included any adjustment of the refractive index for the influence of the thin film of C_{60}.

For the photoexcited case, we can extract the complex conductivity of the sample at particular delay time τ. To this end, we follow the procedure applied previously in a study of transient conductivity in graphene[57] in which we measure the change in the transmitted THz field induced by photoexcitation $\Delta E_\tau(t)$ and the field transmitted through the unexcited sample, $E_0(t)$. Assuming a small differential change of the THz field caused by weak perturbation, we can calculate the change in conductivity from the corresponding Fourier transforms using a linearized version of equation 1, namely,[80,83]

$$\Delta\sigma_\tau(\omega) = -\frac{n+1}{Z_0}\frac{\Delta E_\tau(\omega)}{E_0(\omega)} \quad (4)$$

Here, $\Delta E_\tau(\omega)$ and $E_0(\omega)$ are the Fourier transforms of the corresponding time-domain signals. This expression is valid when the perturbation to the THz response is slight and absorption from the substrate relatively weak (<20%).[84] Both conditions are fulfilled in our measurements.

Conflict of Interest: The authors declare no competing financial interest.

Acknowledgment. We acknowledge support from the National Science Foundation for the optical measurements under grant number DMR-1411107 and for sample preparation under grant number DMR-1122594. The results were analyzed with support from the Office of Naval Research and from the AMOS program, Chemical Sciences, Geosciences, and Biosciences Division, Basic Energy Sciences, U.S. Department of Energy under Contract No. DE-AC02-76-SFO0515 (T.F.H.). G.J. gratefully acknowledges support from the Alexander-von-Humboldt Foundation through a Feodor-Lynen Fellowship. The authors would also like to thank Dr. Steffen Jockusch at Columbia University for his help with absorbance measurements and Dr. Ted Heilweil at NIST for fruitful discussions.

Supporting Information Available: Surface morphology of C_{60} films by atomic force microscope, thickness dependent optical absorbance of C_{60} films, transient THz conductivity response of C_{60} film following 400 and 800 nm laser excitation are presented in Figures S1−S3. The Supporting Information is available free of charge on the ACS Publications website at DOI: 10.1021/acsnano.5b01896.

REFERENCES AND NOTES

1. Katsnelson, M. I.: *Graphene: Carbon in Two Dimensions*; Cambridge University Press: Cambridge, U.K., 2012.
2. Ju, L.; Geng, B.; Horng, J.; Girit, C.; Martin, M.; Hao, Z.; Bechtel, H. A.; Liang, X.; Zettl, A.; Shen, Y. R.; et al. Graphene Plasmonics for Tunable Terahertz Metamaterials. *Nat. Nanotechnol.* **2011**, *6*, 630.
3. Bonaccorso, F.; Sun, Z.; Hasan, T.; Ferrari, A. C. Graphene Photonics and Optoelectronics. *Nat. Photonics* **2010**, *4*, 611.
4. Lemme, M. C.; Echtermeyer, T. J.; Baus, M.; Kurz, H. A Graphene Field-Effect Device. *IEEE Electron Device Lett.* **2007**, *28*, 282.
5. Jablan, M.; Buljan, H.; Soljačić, M. Plasmonics in Graphene at Infrared Frequencies. *Phys. Rev. B* **2009**, *80*, 245435.
6. Lin, Y. M.; Dimitrakopoulos, C.; Jenkins, K. A.; Farmer, D. B.; Chiu, H. Y.; Grill, A.; Avouris, P. 100-Ghz Transistors from Wafer-Scale Epitaxial Graphene. *Science* **2010**, *327*, 662.
7. Liao, L.; Lin, Y.-C.; Bao, M.; Cheng, R.; Bai, J.; Liu, Y.; Qu, Y.; Wang, K. L.; Huang, Y.; Duan, X. High-Speed Graphene Transistors with a Self-Aligned Nanowire Gate. *Nature* **2010**, *467*, 305.
8. Avouris, P. Graphene: Electronic and Photonic Properties and Devices. *Nano Lett.* **2010**, *10*, 4285.
9. Bao, Q.; Loh, K. P. Graphene Photonics, Plasmonics, and Broadband Optoelectronic Devices. *ACS Nano* **2012**, *6*, 3677.
10. Liu, Z. F.; Liu, Q.; Huang, Y.; Ma, Y. F.; Yin, S. G.; Zhang, X. Y.; Sun, W.; Chen, Y. S. Organic Photovoltaic Devices Based on a Novel Acceptor Material: Graphene. *Adv. Mater.* **2008**, *20*, 3924.
11. Guo, C. X.; Yang, H. B.; Sheng, Z. M.; Lu, Z. S.; Song, Q. L.; Li, C. M. Layered Graphene/Quantum Dots for Photovoltaic Devices. *Angew. Chem., Int. Ed.* **2010**, *122*, 3078.
12. Yin, Z.; Zhu, J.; He, Q.; Cao, X.; Tan, C.; Chen, H.; Yan, Q.; Zhang, H. Graphene-Based Materials for Solar Cell Applications. *Adv. Energy Mater.* **2014**, *4*, 1–19.
13. Mak, K. F.; Sfeir, M. Y.; Wu, Y.; Lui, C. H.; Misewich, J. A.; Heinz, T. F. Measurement of the Optical Conductivity of Graphene. *Phys. Rev. Lett.* **2008**, *101*, 196405.
14. Nair, R. R.; Blake, P.; Grigorenko, A. N.; Novoselov, K. S.; Booth, T. J.; Stauber, T.; Peres, N. M. R.; Geim, A. K. Fine Structure Constant Defines Visual Transparency of Graphene. *Science* **2008**, *320*, 1308.
15. Di, C.-a.; Wei, D.; Yu, G.; Liu, Y.; Guo, Y.; Zhu, D. Patterned Graphene as Source/Drain Electrodes for Bottom-Contact Organic Field-Effect Transistors. *Adv. Mater.* **2008**, *20*, 3289.
16. Torrisi, F.; Hasan, T.; Wu, W.; Sun, Z.; Lombardo, A.; Kulmala, T. S.; Hsieh, G.-W.; Jung, S.; Bonaccorso, F.; Paul, P. J.; et al. Inkjet-Printed Graphene Electronics. *ACS Nano* **2012**, *6*, 2992.
17. Secor, E. B.; Prabhumirashi, P. L.; Puntambekar, K.; Geier, M. L.; Hersam, M. C. Inkjet Printing of High Conductivity, Flexible Graphene Patterns. *J. Phys. Chem. Lett.* **2013**, *4*, 1347.
18. Geim, A. K.; Novoselov, K. S. The Rise of Graphene. *Nat. Mater.* **2007**, *6*, 183.
19. Zhang, Y.; Tan, Y.-W.; Stormer, H. L.; Kim, P. Experimental Observation of the Quantum Hall Effect and Berry's Phase in Graphene. *Nature* **2005**, *438*, 201.
20. Klitzing, K. v.; Dorda, G.; Pepper, M. New Method for High-Accuracy Determination of the Fine-Structure Constant Based on Quantized Hall Resistance. *Phys. Rev. Lett.* **1980**, *45*, 494.

21. Heersche, H. B.; Jarillo-Herrero, P.; Oostinga, J. B.; Vandersypen, L. M. K.; Morpurgo, A. F. Bipolar Supercurrent in Graphene. *Nature* **2007**, *446*, 56.
22. Malig, J.; Jux, N.; Kiessling, D.; Cid, J. J.; Vazquez, P.; Torres, T.; Guldi, D. M. Towards Tunable Graphene/Phthalocyanine-Ppv Hybrid Systems. *Angew. Chem., Int. Ed.* **2011**, *50*, 3561.
23. Dai, L. M.; Chang, D. W.; Baek, J. B.; Lu, W. Carbon Nanomaterials for Advanced Energy Conversion and Storage. *Small* **2012**, *8*, 1130.
24. Park, W.; Lee, J.; Lee, D.; Yi, G.-C. Hybrid Semiconductor Nanostructures with Graphene Layers. In *Semiconductor Nanostructures for Optoelectronic Devices*; Yi, G.-C., Ed.; Nanoscience and Technology; Springer: Berlin, Germany, 2012; p 167.
25. Stankovich, S.; Dikin, D. A.; Dommett, G. H. B.; Kohlhaas, K. M.; Zimney, E. J.; Stach, E. A.; Piner, R. D.; Nguyen, S. T.; Ruoff, R. S. Graphene-Based Composite Materials. *Nature* **2006**, *442*, 282.
26. Konstantatos, G.; Badioli, M.; Gaudreau, L.; Osmond, J.; Bernechea, M.; de Arquer, F. P. G.; Gatti, F.; Koppens, F. H. L. Hybrid Graphene-Quantum Dot Phototransistors with Ultrahigh Gain. *Nat. Nanotechnol.* **2012**, *7*, 363.
27. Cox, M.; Gorodetsky, A.; Kim, B.; Kim, K. S.; Jia, Z.; Kim, P.; Nuckolls, C.; Kymissis, I. Single-Layer Graphene Cathodes for Organic Photovoltaics. *Appl. Phys. Lett.* **2011**, *98*, 123303.
28. Cho, J.; Smerdon, J.; Gao, L.; Süzer, Ö.; Guest, J. R.; Guisinger, N. P. Structural and Electronic Decoupling of C_{60} from Epitaxial Graphene on Sic. *Nano Lett.* **2012**, *12*, 3018.
29. Švec, M.; Merino, P.; Dappe, Y. J.; González, C.; Abad, E.; Jelínek, P.; Martín-Gago, J. A. van der Waals Interactions Mediating the Cohesion of Fullerenes on Graphene. *Phys. Rev. B* **2012**, *86*, 121407.
30. Jeon, E. K.; Yang, C. S.; Shen, Y. F.; Nakanishi, T.; Jeong, D. S.; Kim, J. J.; Ahn, K. S.; Kong, K. J.; Lee, J. O. Photoconductivity and Enhanced Memory Effects in Hybrid C_{60}-Graphene Transistors. *Nanotechnology* **2012**, *23*.
31. Wang, R.; Wang, S.; Wang, X.; Meyer, J. A. S.; Hedegård, P.; Laursen, B. W.; Cheng, Z.; Qiu, X. Charge Transfer and Current Fluctuations in Single Layer Graphene Transistors Modified by Self-Assembled C_{60} Adlayers. *Small* **2013**, *9*, 2420.
32. Yi, Y.; Choi, W. M.; Son, B.; Kim, J. W.; Kang, S. J. Interfacial Electronic Structures between Fullerene and Multilayer Graphene for N-Type Organic Semiconducting Devices. *Carbon* **2011**, *49*, 4936.
33. Wudl, F. Fullerene Materials. *J. Mater. Chem.* **2002**, *12*, 1959.
34. Yu, D. S.; Park, K.; Durstock, M.; Dai, L. M. Fullerene-Grafted Graphene for Efficient Bulk Heterojunction Polymer Photovoltaic Devices. *J. Phys. Chem. Lett.* **2011**, *2*, 1113.
35. Ferrari, A. C.; Meyer, J. C.; Scardaci, V.; Casiraghi, C.; Lazzeri, M.; Mauri, F.; Piscanec, S.; Jiang, D.; Novoselov, K. S.; Roth, S.; et al. Raman Spectrum of Graphene and Graphene Layers. *Phys. Rev. Lett.* **2006**, *97*, 187401.
36. Dresselhaus, M. S.; Dresselhaus, G.; Eklund, P. C. *Science of Fullerenes and Carbon Nanotubes*; Academic Press, Inc.: San Diego, CA, 1996.
37. Das, A.; Pisana, S.; Chakraborty, B.; Piscanec, S.; Saha, S. K.; Waghmare, U. V.; Novoselov, K. S.; Krishnamurthy, H. R.; Geim, A. K.; Ferrari, A. C.; et al. Monitoring Dopants by Raman Scattering in an Electrochemically Top-Gated Graphene Transistor. *Nat. Nanotechnol.* **2008**, *3*, 210.
38. Pisana, S.; Lazzeri, M.; Casiraghi, C.; Novoselov, K. S.; Geim, A. K.; Ferrari, A. C.; Mauri, F. Breakdown of the Adiabatic Born-Oppenheimer Approximation in Graphene. *Nat. Mater.* **2007**, *6*, 198.
39. Yan, J.; Zhang, Y. B.; Kim, P.; Pinczuk, A. Electric Field Effect Tuning of Electron-Phonon Coupling in Graphene. *Phys. Rev. Lett.* **2007**, *98*, 166802.
40. Kalbac, M.; Reina-Cecco, A.; Farhat, H.; Kong, J.; Kavan, L.; Dresselhaus, M. S. The Influence of Strong Electron and Hole Doping on the Raman Intensity of Chemical Vapor-Deposition Graphene. *ACS Nano* **2010**, *4*, 6055.
41. Chen, C.-F.; Park, C.-H.; Boudouris, B. W.; Horng, J.; Geng, B.; Girit, C.; Zettl, A.; Crommie, M. F.; Segalman, R. A.; Louie, S. G.; et al. Controlling Inelastic Light Scattering Quantum Pathways in Graphene. *Nature* **2011**, *471*, 617.
42. Zhang, Y. B.; Tan, Y. W.; Stormer, H. L.; Kim, P. Experimental Observation of the Quantum Hall Effect and Berry's Phase in Graphene. *Nature* **2005**, *438*, 201.
43. Lee, J. E.; Ahn, G.; Shim, J.; Lee, Y. S.; Ryu, S. Optical Separation of Mechanical Strain from Charge Doping in Graphene. *Nat. Commun.* **2012**, *3*, 1024.
44. Tielrooij, K. J.; Song, J. C. W.; Jensen, S. A.; Centeno, A.; Pesquera, A.; Elorza, A. Z.; Bonn, M.; Levitov, L. S.; Koppens, F. H. L. Photoexcitation Cascade and Multiple Hot-Carrier Generation in Graphene. *Nat. Phys.* **2013**, *9*, 248.
45. Tomaino, J. L.; Jameson, A. D.; Kevek, J. W.; Paul, M. J.; van der Zande, A. M.; Barton, R. A.; McEuen, P. L.; Minot, E. D.; Lee, Y.-S. Terahertz Imaging and Spectroscopy of Large-Area Single-Layer Graphene. *Opt. Express* **2011**, *19*, 141.
46. Maeng, I.; Lim, S.; Chae, S. J.; Lee, Y. H.; Choi, H.; Son, J. H. Gate-Controlled Nonlinear Conductivity of Dirac Fermion in Graphene Field-Effect Transistors Measured by Terahertz Time-Domain Spectroscopy. *Nano Lett.* **2012**, *12*, 551.
47. Buron, J. D.; Pizzocchero, F.; Jessen, B. S.; Booth, T. J.; Nielsen, P. F.; Hansen, O.; Hilke, M.; Whiteway, E.; Jepsen, P. U.; Boggild, P.; et al. Electrically Continuous Graphene from Single Crystal Copper Verified by Terahertz Conductance Spectroscopy and Micro Four-Point Probe. *Nano Lett.* **2014**, *14*, 6348.
48. Hwang, E. H.; Adam, S.; Das Sarma, S. Carrier Transport in Two-Dimensional Graphene Layers. *Phys. Rev. Lett.* **2007**, *98*, 186806.
49. Nomura, K.; MacDonald, A. H. Quantum Transport of Massless Dirac Fermions. *Phys. Rev. Lett.* **2007**, *98*, 076602.
50. Peres, N. M. R.; Lopes dos Santos, J. M. B.; Stauber, T. Phenomenological Study of the Electronic Transport Coefficients of Graphene. *Phys. Rev. B* **2007**, *76*, 073412.
51. Castro Neto, A. H.; Guinea, F.; Peres, N. M. R.; Novoselov, K. S.; Geim, A. K. The Electronic Properties of Graphene. *Rev. Mod. Phys.* **2009**, *81*, 109.
52. Ando, T. Screening Effect and Impurity Scattering in Monolayer Graphene. *J. Phys. Soc. Jpn.* **2006**, *75*, 074716.
53. Gusynin, V. P.; Sharapov, S. G. Transport of Dirac Quasiparticles in Graphene: Hall and Optical Conductivities. *Phys. Rev. B* **2006**, *73*, 245411.
54. Gusynin, V. P.; Sharapov, S. G.; Carbotte, J. P. On the Universal Ac Optical Background in Graphene. *New J. Phys.* **2009**, *11*, 095013.
55. Stauber, T.; Peres, N. M. R.; Guinea, F. Electronic Transport in Graphene: A Semiclassical Approach Including Midgap States. *Phys. Rev. B* **2007**, *76*, 205423.
56. Lane, P. A.; Cunningham, P. D.; Melinger, J. S.; Kushto, G. P.; Esenturk, O.; Heilweil, E. J. Photoexcitation Dynamics in Films of C_{60} and Zn Phthalocyanine with a Layered Nanostructure. *Phys. Rev. Lett.* **2012**, *108*, 077402.
57. Jnawali, G.; Rao, Y.; Yan, H.; Heinz, T. F. Observation of a Transient Decrease in Terahertz Conductivity of Single-Layer Graphene Induced by Ultrafast Optical Excitation. *Nano Lett.* **2013**, *13*, 524.
58. Liu, H.; Reinke, P. C-60 Thin Film Growth on Graphite: Coexistence of Spherical and Fractal-Dendritic Islands. *J. Chem. Phys.* **2006**, *124*, No. 164707.
59. Li, G.; Zhou, H. T.; Pan, L. D.; Zhang, Y.; Mao, J. H.; Zou, Q.; Guo, H. M.; Wang, Y. L.; Du, S. X.; Gao, H. J. Self-Assembly of C_{60} Monolayer on Epitaxially Grown, Nanostructured Graphene on Ru(0001) Surface. *Appl. Phys. Lett.* **2012**, *100*, 013304.
60. Das Sarma, S.; Adam, S.; Hwang, E. H.; Rossi, E. Electronic Transport in Two-Dimensional Graphene. *Rev. Mod. Phys.* **2011**, *83*, 407.
61. Hamed, A.; Sun, Y. Y.; Tao, Y. K.; Meng, R. L.; Hor, P. H. Effects of Oxygen and Illumination on the *in Situ* Conductivity of C_{60} Thin Films. *Phys. Rev. B* **1993**, *47*, 10873.
62. Lee, C. H.; Yu, G.; Kraabel, B.; Moses, D.; Srdanov, V. I. Effects of Oxygen on the Photocarrier Dynamics in a

C_{60} Film: Studies of Transient and Steady-State Photoconductivity. *Phys. Rev. B* **1994**, *49*, 10572.
63. Owens, D. W.; Aldao, C. M.; Poirier, D. M.; Weaver, J. H. Charge Transfer, Doping, and Interface Morphologies for Al-C_{60}. *Phys. Rev. B* **1995**, *51*, 17068.
64. Tjeng, L. H.; Hesper, R.; Heessels, A. C. L.; Heeres, A.; Jonkman, H. T.; Sawatzky, G. A. Development of the Electronic Structure in a K-Doped C_{60} Monolayer on a Ag(111) Surface. *Solid State Commun.* **1997**, *103*, 31.
65. Tzeng, C. T.; Lo, W. S.; Yuh, J. Y.; Chu, R. Y.; Tsuei, K. D. Photoemission, near-Edge X-ray-Absorption Spectroscopy, and Low-Energy Electron-Diffraction Study of C_{60} on Au(111) Surfaces. *Phys. Rev. B* **2000**, *61*, 2263.
66. Frenzel, A. J.; Lui, C. H.; Fang, W.; Nair, N. L.; Herring, P. K.; Jarillo-Herrero, P.; Kong, J.; Gedik, N. Observation of Suppressed Terahertz Absorption in Photoexcited Graphene. *Appl. Phys. Lett.* **2013**, *102*, 113111.
67. Shi, S. F.; Tang, T. T.; Zeng, B.; Ju, L.; Zhou, Q.; Zettl, A.; Wang, F. Controlling Graphene Ultrafast Hot Carrier Response from Metal-like to Semiconductor-Like by Electrostatic Gating. *Nano Lett.* **2014**, *14*, 1578.
68. Sarkar, D.; Halas, N. J. Dember Effect in C_{60} Thin Films. *Solid State Commun.* **1994**, *90*, 261.
69. Tapponnier, A.; Biaggio, I.; Gunter, P. Ultrapure C_{60} Field-Effect Transistors and the Effects of Oxygen Exposure. *Appl. Phys. Lett.* **2005**, *86*, 112114.
70. Chen, Z. Y.; Berciaud, S.; Nuckolls, C.; Heinz, T. F.; Brus, L. E. Energy Transfer from Individual Semiconductor Nanocrystals to Graphene. *ACS Nano* **2010**, *4*, 2964.
71. Li, X.; Cai, W.; An, J.; Kim, S.; Nah, J.; Yang, D.; Piner, R.; Velamakanni, A.; Jung, I.; Tutuc, E.; et al. Large-Area Synthesis of High-Quality and Uniform Graphene Films on Copper Foils. *Science* **2009**, *324*, 1312.
72. Petrone, N.; Dean, C. R.; Meric, I.; van der Zande, A. M.; Huang, P. Y.; Wang, L.; Muller, D.; Shepard, K. L.; Hone, J. Chemical Vapor Deposition-Derived Graphene with Electrical Performance of Exfoliated Graphene. *Nano Lett.* **2012**, *12*, 2751.
73. Luo, M. F.; Li, Z. Y.; Allison, W. Initial Stages of C60 Thin Film Growth on Graphite. *Surf. Sci.* **1998**, *402−404*, 437–440.
74. Kenny, D. J.; Palmer, R. E. Nucleation and Growth of C60 Thin Films on Graphite. *Surf. Sci.* **2000**, *447*, 126.
75. Ulbricht, R.; Hendry, E.; Shan, J.; Heinz, T. F.; Bonn, M. Carrier Dynamics in Semiconductors Studied with Time-Resolved Terahertz Spectroscopy. *Rev. Mod. Phys.* **2011**, *83*, 543.
76. Nahata, A.; Auston, D. H.; Heinz, T. F.; Wu, C. J. Coherent Detection of Freely Propagating Terahertz Radiation by Electro-Optic Sampling. *Appl. Phys. Lett.* **1996**, *68*, 150.
77. Wu, Q.; Zhang, X. C. Free-Space Electro-Optic Sampling of Terahertz Beams. *Appl. Phys. Lett.* **1995**, *67*, 3523.
78. Nahata, A.; Weling, A. S.; Heinz, T. F. A Wideband Coherent Terahertz Spectroscopy System Using Optical Rectification and Electro-Optic Sampling. *Appl. Phys. Lett.* **1996**, *69*, 2321.
79. Tinkham, M. Energy Gap Interpretation of Experiments on Infrared Transmission through Superconducting Films. *Phys. Rev. B* **1956**, *104*, 845.
80. Hegmann, F. A.; Ostroverkhova, O.; Cooke, D. G.: Probing Organic Semiconductors with Terahertz Pulses. In *Photophysics of Molecular Materials*; Wiley-VCH Verlag GmbH & Co. KGaA: Weinheim, Germany, 2006.
81. Parker, T. J.; Ford, J. E.; Chambers, W. G. The Optical Constants of Pure Fused Quartz in the Far-Infrared. *Infrared Phys.* **1978**, *18*, 215.
82. Naftaly, M.; Miles, R. E. Terahertz Time-Domain Spectroscopy for Material Characterization. *Proc. IEEE* **2007**, *95*, 1658.
83. Nienhuys, H.-K.; Sundström, V. Intrinsic Complications in the Analysis of Optical-Pump, Terahertz Probe Experiments. *Phys. Rev. B* **2005**, *71*, 235110.
84. Knoesel, E.; Bonn, M.; Shan, J.; Wang, F.; Heinz, T. F. Conductivity of Solvated Electrons in Hexane Investigated with Terahertz Time-Domain Spectroscopy. *J. Chem. Phys.* **2004**, *121*, 394.